Electronic Supplementary Information

K^+ Pre-intercalated Manganese Dioxide with Enhanced Zn^{2+} Diffusion for High Rate and Durable Aqueous Zinc-Ion Battery

Guoxue Liu,‡[a] Huawen Huang,‡[a] Ran Bi,[a] Xue Xiao,[b] Tianyi Ma,*[b] and Lei Zhang*[a]

[a] *School of Chemistry & Chemical Engineering, South China University of Technology, Guangzhou 510640, P. R. China. E-mail: celeizhang@scut.edu.cn*

[b] *Discipline of Chemistry, The University of Newcastle, Callaghan, NSW 2308, Australia. E-mail: tianyi.ma@newcastle.edu.au*

‡*These authors contributed equally to the work.*

1. Experimental Section

1.1 Synthesis of carbon nanofibers

0.9 g of polyacrylonitrile (PAN, Mw ~150,000) was dissolved in 9.1 g of *N,N*-dimethylformamide (DMF) to prepare PAN nanofibers and the mixed solution was stirred vigorously for 24 h at 60 ^{o}C. Then, the as-prepared solution was loaded into a syringe with a stainless needle, which was applied with a high voltage of 15 kV, and the distance between the nozzle and the collector was 16 cm with a feed rate of 1 mL h^{-1}. Finally, the as-spun PAN nanofibers were heated at 280 ^{o}C for 3 h at a heating rate of 1 ^{o}C min^{-1} in air and then the as-stabilized nanofibers were carbonized at 800 ^{o}C for 3 h at a heating rate of 5 ^{o}C min^{-1} under an Argon atmosphere.

1.2 Synthesis of α-$K_{0.19}MnO_2$ nanotubes

100 mg of $KMnO_4$ were dissolved into 60 mL of deionized water with stirring for 1 h. Subsequently, the carbon nanofibers film was cut into slices (2 × 2 cm) and the carbon nanofibers slice was immersed into the $KMnO_4$ aqueous solution. The as-prepared solution with carbon nanofibers slice was transferred into a 100 mL Teflon-lined stainless-steel autoclave and kept at 140 ^{o}C for 10 h in an oven. The brown slice was obtained and washed with water and ethanol for several times, and then dried at 60 ^{o}C overnight. Finally, the brown slice was heated to 500 ^{o}C for 3 h at a heating rate of 10 ^{o}C min^{-1} under air to obtain the α-$K_{0.19}MnO_2$ nanotubes. The α-$K_{0.07}MnO_2$ nanotubes were obtained *via* concentrated HNO_3 treatment.[S1]

1.3 Materials characterization

Field emission scanning electron microscopy (FESEM, SU8220, 5 kV) and transmission electron microscopy (TEM, JEM-2100F, 200 kV) were used to characterize the morphologies and structures of all samples. The crystal structures of all samples were examined by X-ray diffraction (XRD, Bruker D8 ADVANCE, 40 kV, 40 mA) with Cu Kα radiation (λ = 1.54 Å). Compositions of the samples were measured by inductively coupled plasma optical emission

spectroscopy (ICP-OES, Agilent 720), X-ray photoelectron spectroscopy (XPS, Thermo Scientific Escalab 250Xi), thermogravimetric analysis (TGA, NETZSCH STA449 F5) and energy-dispersive X-ray (EDX, Oxford Instruments) spectroscopy attached to the SEM instrument. The nitrogen adsorption/desorption isotherms of all samples were collected at 77 K by a Micromeritics 3Flex instrument.

1.4 Electrochemical measurements

The electrode was fabricated by mixing the active material (α-$K_{0.19}MnO_2$ and α-$K_{0.07}MnO_2$ nanotubes), Super-P, and polytetrafluoroethylene (PTFE) with a mass ratio of 7:2:1 using isopropanol as a solvent, and then the electrode slurry was casted on a titanium disc at a mass loading of around 1.0 mg cm^{-2} and vacuum-dried at 60 ^{o}C overnight. The electrochemical properties were investigated in CR2032 coin-type cells using zinc metal foil as the anode, glass fiber (Whatman, GF/F) membrane as the separator. The Zn foil with a thickness of 0.1 mm was polished with SiC sandpaper and then cut into small pieces of 15 mm in diameter. And 3 M $Zn(CF_3SO_3)_2$ and 0.2 M $Mn(CF_3SO_3)_2$ with/without 3 M $K(CF_3SO_3)$ as the electrolyte. The cyclic voltammetry (CV) curves were collected on an electrochemical workstation (Gamry 1000E). Galvanostatic discharge–charge tests were examined on a Neware battery measurement system within a voltage window of 0.8−1.9 V. Galvanostatic Intermittent Titration Technique (GITT) was measured by a galvanostatic discharge/charge pulse lasted for 10 min at 50 mA g^{-1} followed by a 60 min relaxation without any current flowing through the cells. Electrochemical impedance spectroscopy (EIS) analysis was obtained on an electrochemical workstation (Gamry 1000E) with a 5 mV AC oscillation amplitude in the frequency ranging from 1 MHz to 10^{-2} Hz.

2. Supplementary Figures

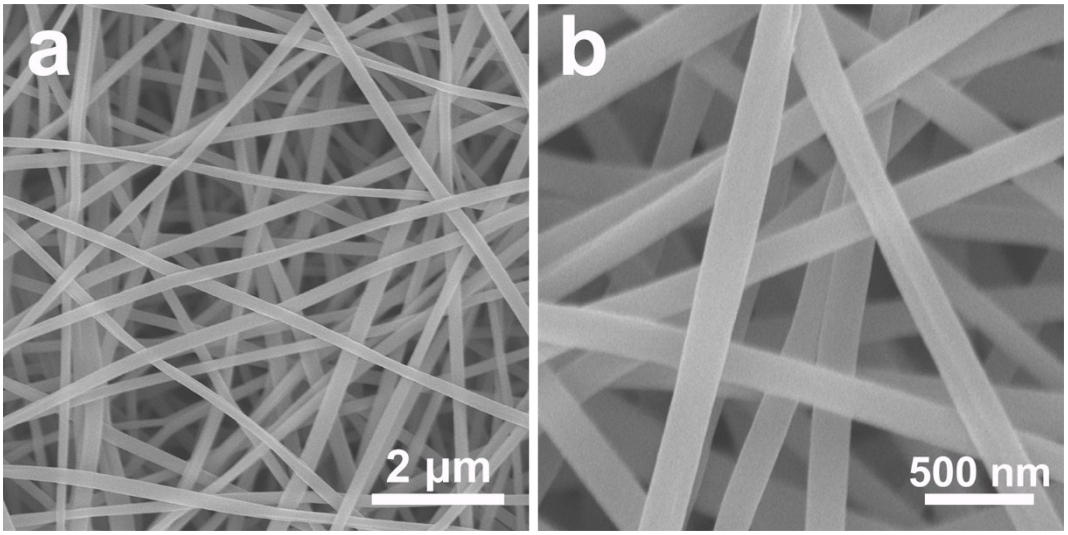

Fig. S1 (a–b) FESEM images of carbon nanofibers.

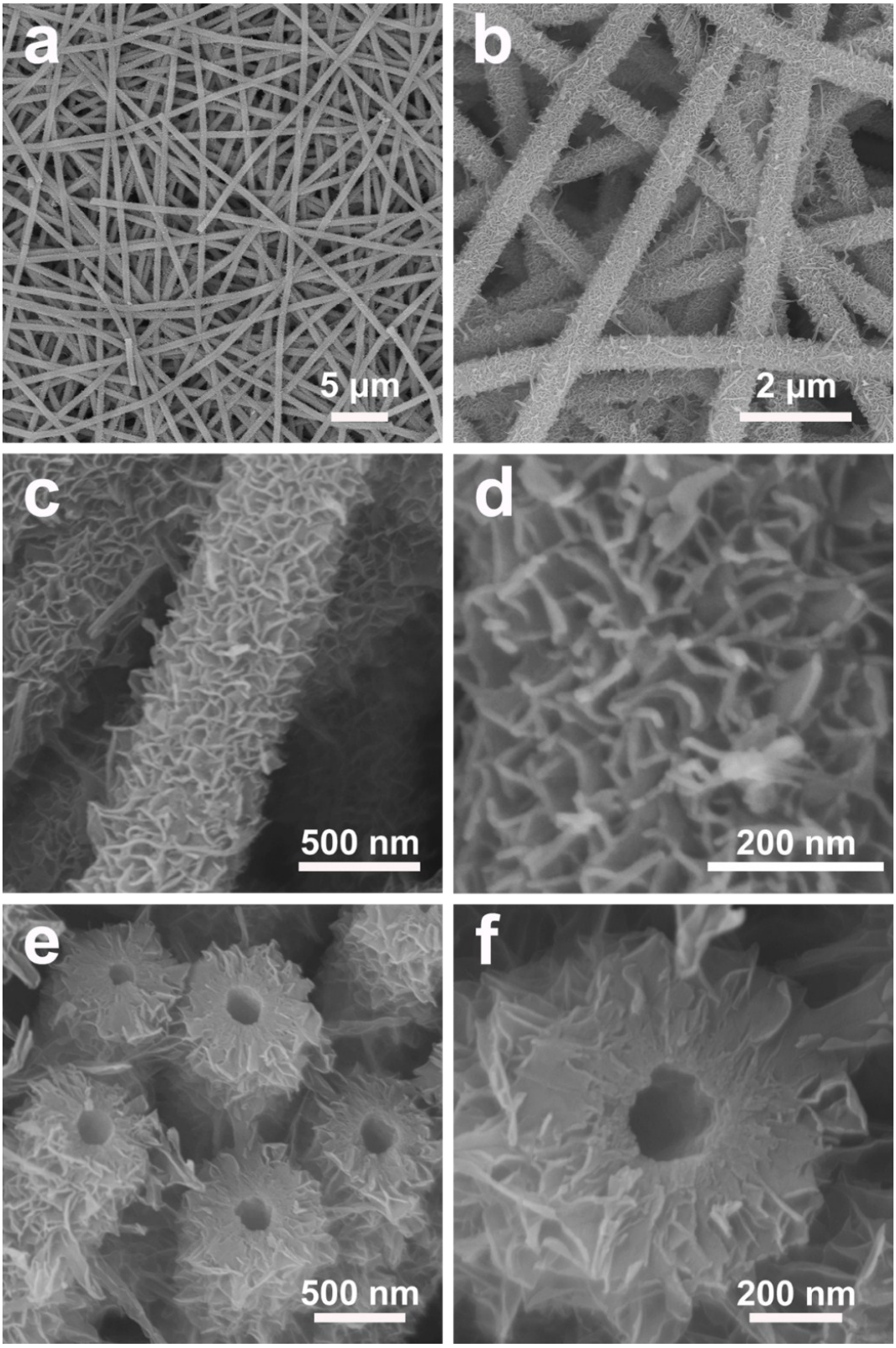

Fig. S2 (a–c) FESEM images of δ-$K_{0.19}MnO_2$ nanotubes at different magnifications. (d) Magnified FESEM image of the surface of δ-$K_{0.19}MnO_2$ nanotubes. (e–f) Cross-sectional FESEM images of the δ-$K_{0.19}MnO_2$ nanobutes.

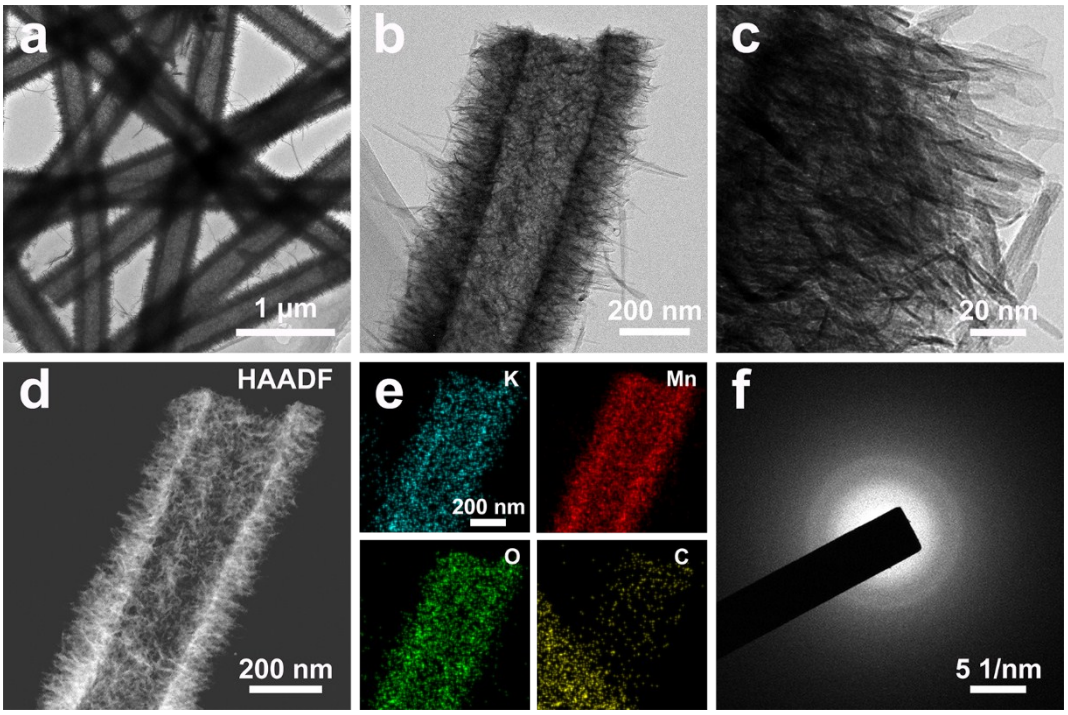

Fig. S3 (a−c) TEM images; (d) HAADF-STEM image; (e) the element mapping images of K, Mn, O, and C; (f) the SAED image of δ-$K_{0.19}MnO_2$ nanotubes.

The TEM and HAADF-STEM images (**Fig. S3a−d**) further elucidate the hollow interior of δ-$K_{0.19}MnO_2$. The element mapping images show the carbon element is few detected in δ-$K_{0.19}MnO_2$ nanotubes, indicating that alomst all of the carbon nanofibers are etched, and the potassium element is uniformly distributed on the nanotubes (**Fig. S3e**). Notably, weak carbon signal was present in the mapping image, which may come from the residual carbon in the δ-$K_{0.19}MnO_2$ nanotubes. In addition, the SAED pattern (**Fig. S3f**) further reveals the polycrystalline nature of the δ-$K_{0.19}MnO_2$ nanotubes.

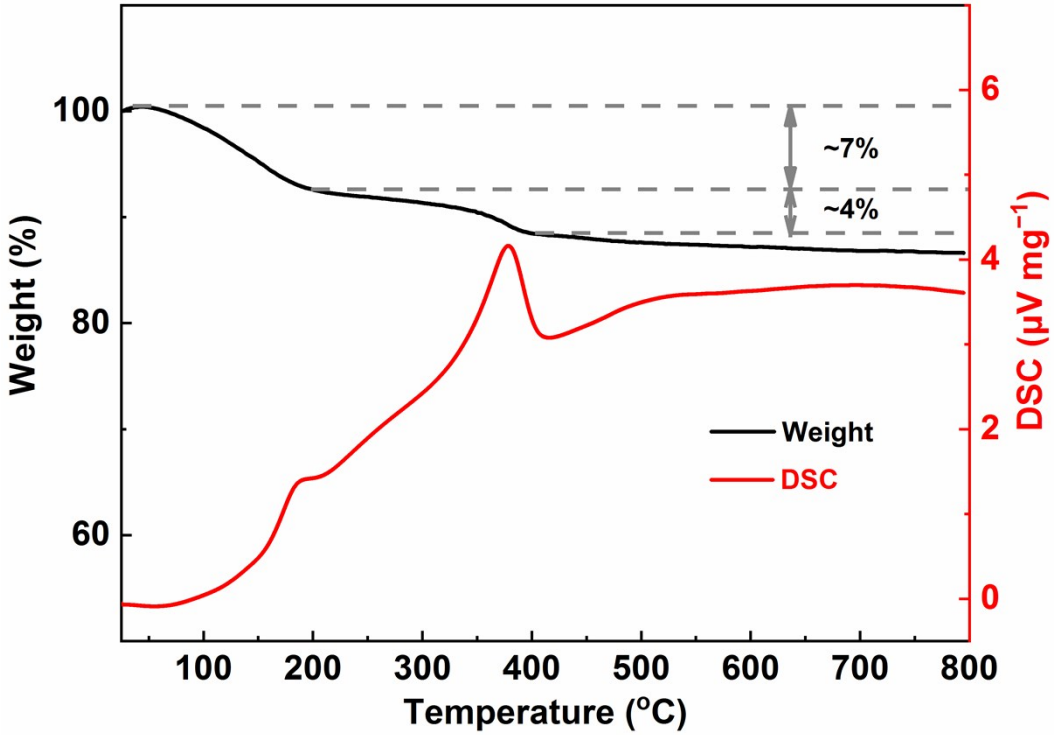

Fig. S4 TGA/DSC simultaneous thermal analysis of δ-$K_{0.19}MnO_2$ nanotubes.

Fig. S4 shows the TGA/DSC curves of δ-$K_{0.19}MnO_2$ nanotubes. The experiment was done with an air atmosphere at a heating speed of 10 °C min^{-1}. The thermogravimetric analysis (TGA) test was applied to investigate mass change of samples during the heat treatment. The results display ~7% weight loss until 190 °C and ~4% weight loss during 200–400 °C, which are attributed to escape of crystal water and remaining carbon in δ-$K_{0.19}MnO_2$ nanotubes, respectively. Therefore, no obvious mass change occurred during the crystal phase transition.

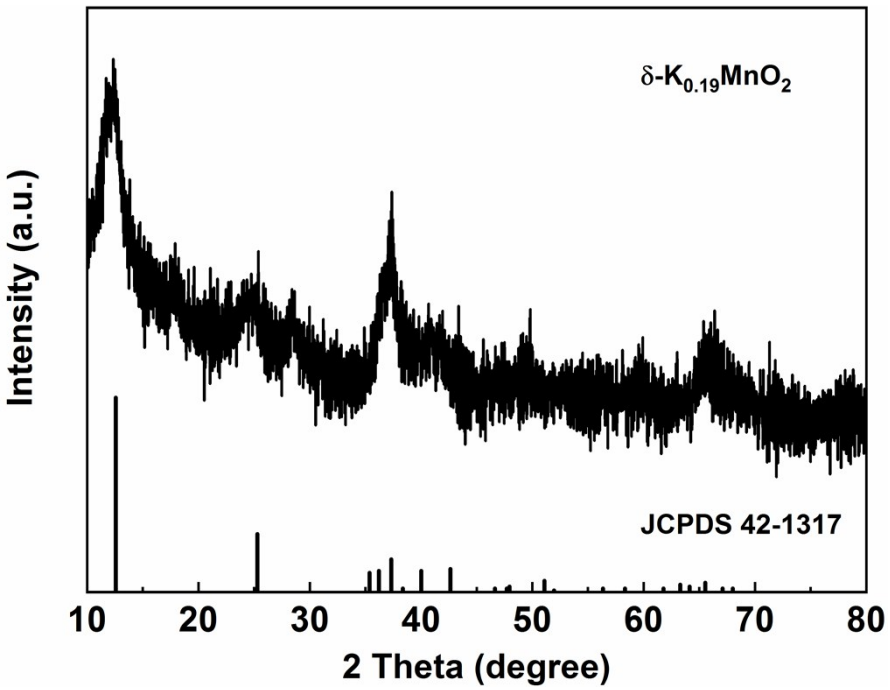

Fig. S5 XRD pattern of δ-$K_{0.19}MnO_2$ nanotubes.

In this work, the α-$K_{0.19}MnO_2$ was obtained through a heat treatment of the δ-$K_{0.19}MnO_2$ nanotubes. Notably, the heat treatment process is heating at 500 ^oC for 3 h with a heating rate of 10 ^oC min^{-1} under air, which is consistent with the heat treatment process of the thermogravimetric analysis (TGA) test (**Fig. S4**). Before the heat treatment, the crystal structure of the material is layered birnessite phase (JCPDS: 42-1317), as shown in **Fig. S5**. After the heat treatment in air, the δ-$K_{0.19}MnO_2$ was transformed into α-$K_{0.19}MnO_2$ (JCPDS: 44-0141), and the corresponding XRD spectrum analysis was shown in **Fig. 2a**. Therefore, from the results of the of XRD, it can be concluded that the crystal structure of δ-$K_{0.19}MnO_2$ will transform into α-$K_{0.19}MnO_2$ after heat treatment in air at 500 ^oC. Furthermore, as exhibited in the TGA curve, the two weight loss processes can be attributed to moisture and remaining carbon, respectively. Meanwhile no obvious mass change occurred during the crystal phase transition.

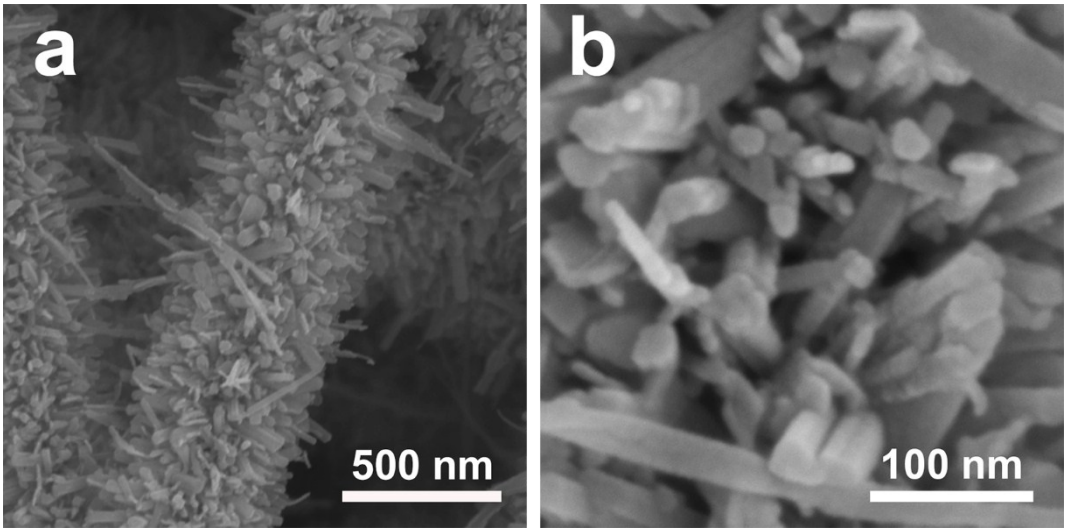

Fig. S6 (a−b) FESEM images of α-$K_{0.19}MnO_2$ nanotubes.

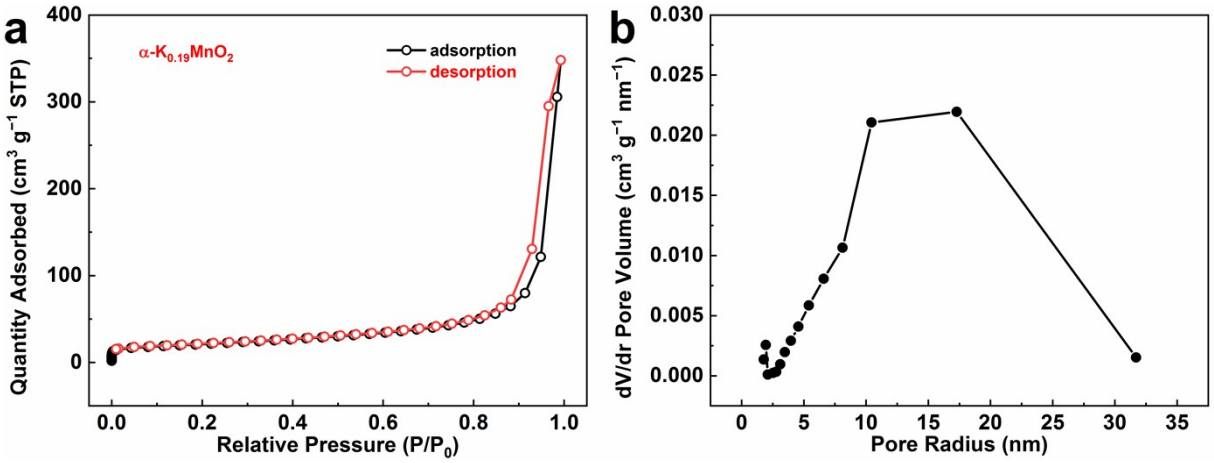

Fig. S7 (a) N_2 adsorption–desorption isotherm and (b) Barrett–Joyner–Halenda (BJH) pore size distribution of α-$K_{0.19}MnO_2$ nanotubes.

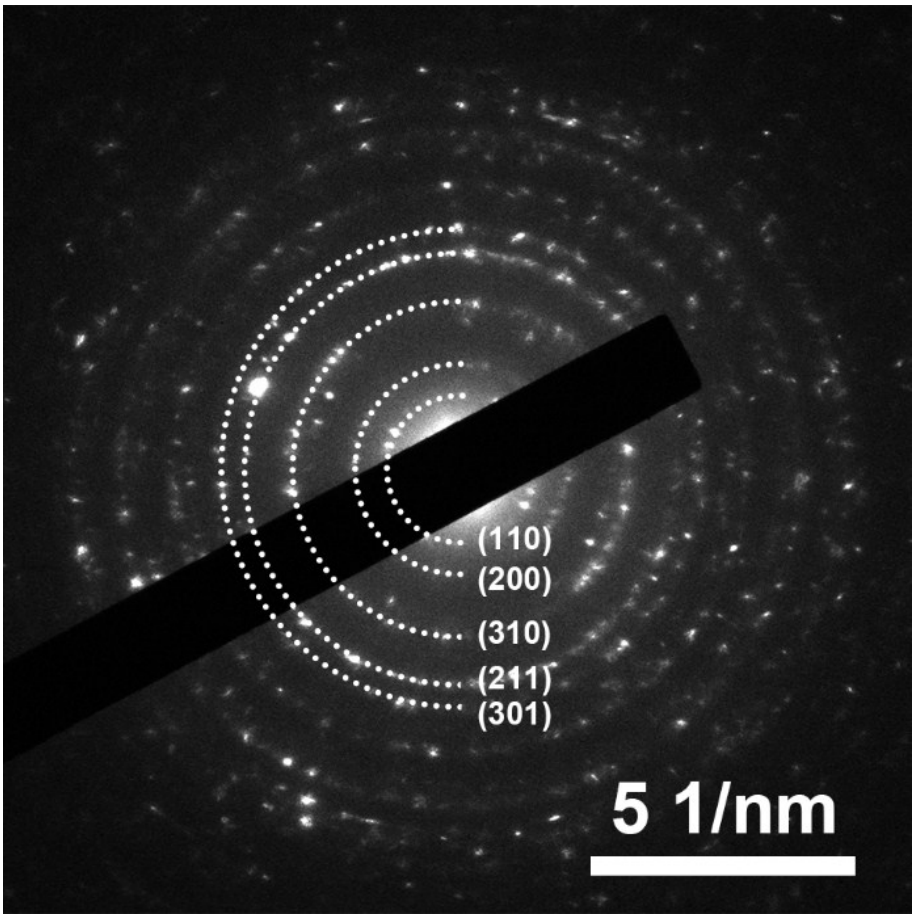

Fig. S8 The selected area electron diffraction (SEAD) image of α-$K_{0.19}MnO_2$ nanotubes.

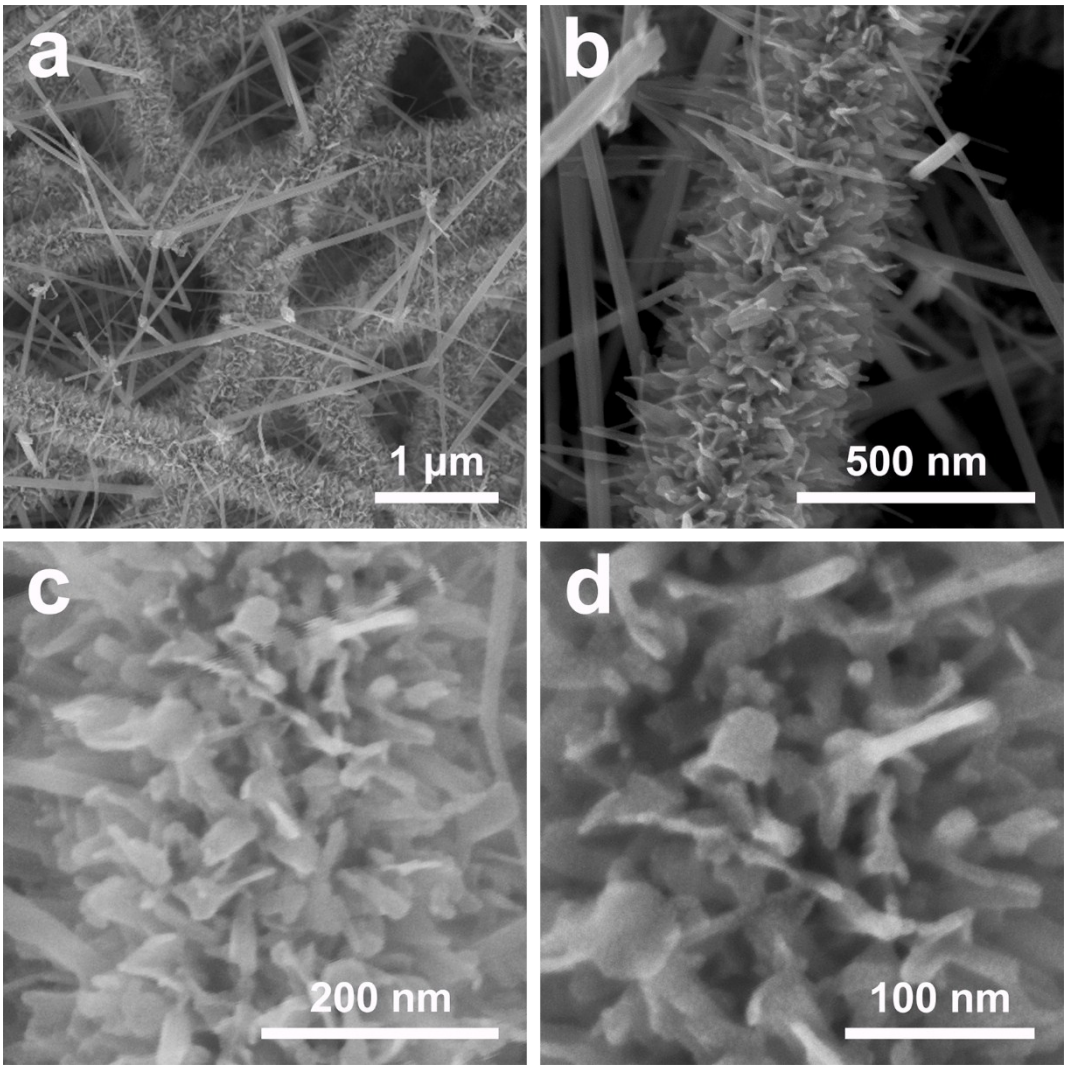

Fig. S9 (a−b) FESEM images of α-$K_{0.07}MnO_2$ nanotubes. (c) FESEM image and (d) magnified FESEM image of the surface of α-$K_{0.07}MnO_2$ nanotubes.

FESEM (**Fig. S9**) images show that the α-$K_{0.07}MnO_2$ nanotubes still retain the hierarchical tubular structures composed of nanorods without obvious changes after K^+ removal.

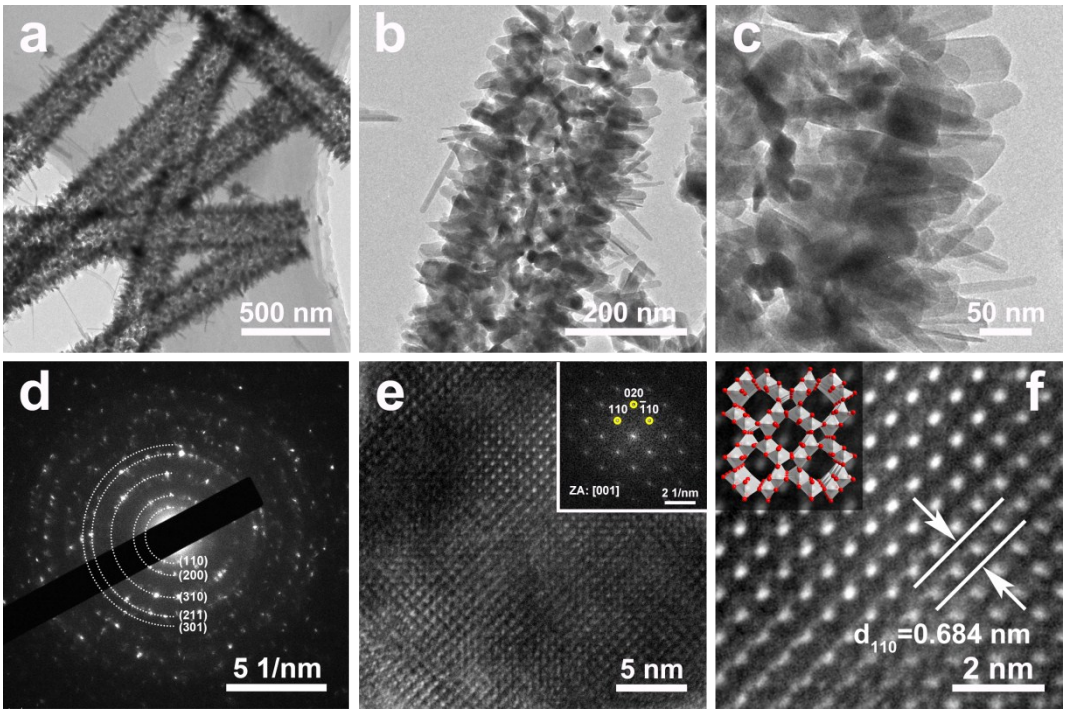

Fig. S10 (a−c) TEM images; (d) the corresponding SEAD image; (e−f) HRTEM images of α-$K_{0.07}MnO_2$ nanotubes. Inset (e): the corresponding FFT [001] electron diffraction pattern; inset (f): the crystal structure of α-MnO_2 without K cations.

The TEM images (**Fig. S10a−c**) indicate that the shell of the nanotubes consists of vertical nanorods forming the porous structure, consistent with the FESEM results. The SEAD results (**Fig. S10d**) deduce the α-$K_{0.07}MnO_2$ still maintain good the tunnel hollandite-type phase. In addition, the 2 × 2 tunnel structures are clearly observed from HRTEM images (**Fig. S10e−f**), but it is noted that the 2 × 2 tunnel structures slightly change after K^+ removal, as indicated by the (110) spacing decreasing from 0.693 to 0.684 nm.

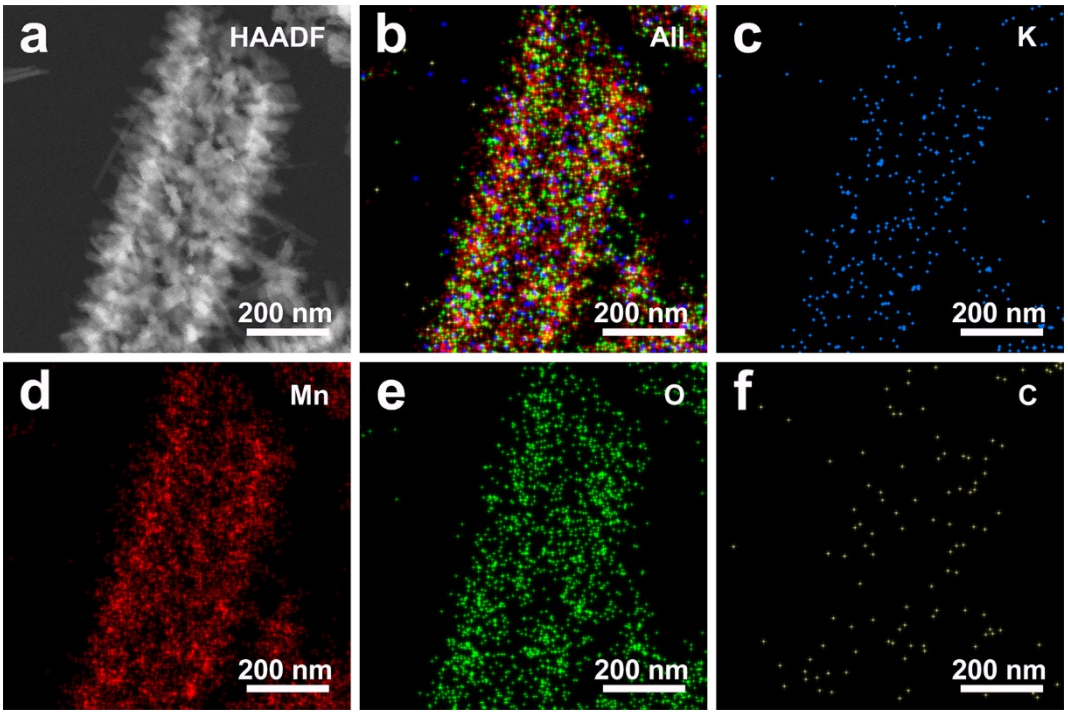

Fig. S11 (a) HAADF; (b) all mixed elements; (c−f) K, Mn, O, and C element, respectively, of α-$K_{0.07}MnO_2$ nanotubes.

The elemental mapping images of α-$K_{0.07}MnO_2$ are shown in **Fig. S11**, indicating the uniform distribution of Mn, O elements and few K^+ signal.

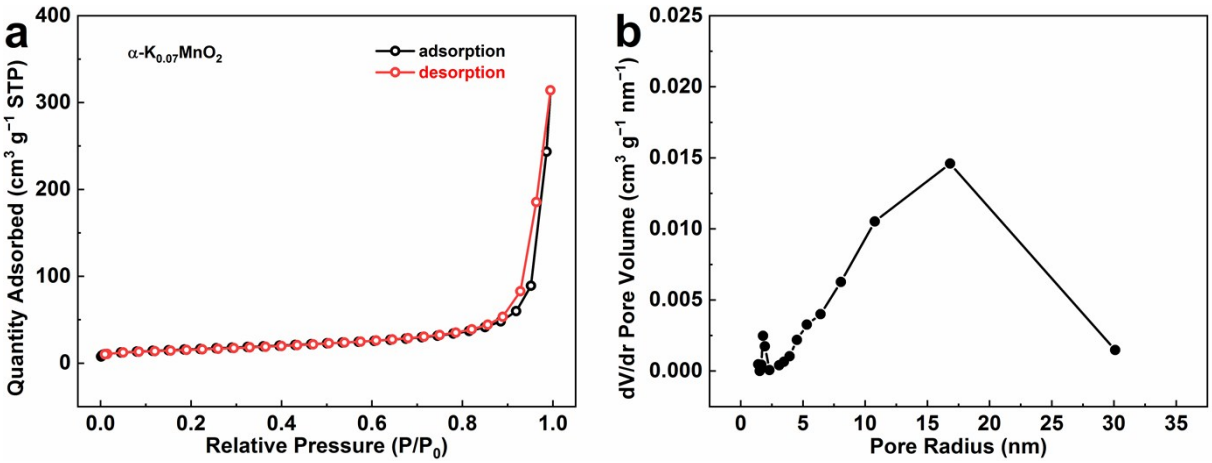

Fig. S12 (a) N_2 adsorption–desorption isotherm and (b) Barrett–Joyner–Halenda (BJH) pore size distribution of α-$K_{0.07}MnO_2$ nanotubes.

The specific surface area (SSA) of α-$K_{0.07}MnO_2$ nanotubes was 56.4 m^2 g^{-1}, which was calculated from N_2 adsorption–desorption isotherm **(Fig. S12)**. And the SSA of α-$K_{0.07}MnO_2$ nanotubes is slightly smaller than that of α-$K_{0.19}MnO_2$ nanotubes (75.3 m^2 g^{-1}), which may be due to the destruction of a small portion of the porous structure in nanotubes during the acid treatment process, resulting in the decrease of specific surface area of α-$K_{0.07}MnO_2$ nanotubes.

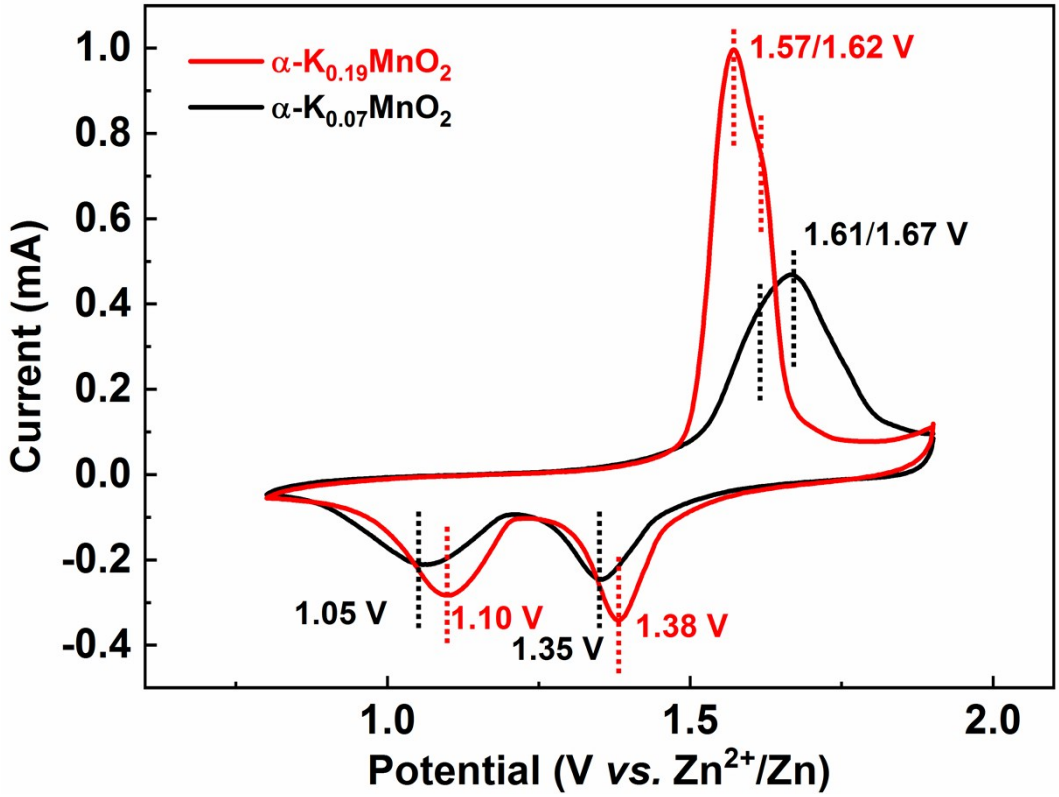

Fig. S13 Comparison of second CV curves of α-$K_{0.19}MnO_2$ and α-$K_{0.07}MnO_2$ cathodes in 3 M $Zn(CF_3SO_3)_2$ and 0.2 M $Mn(CF_3SO_3)_2$ electrolyte.

Fig. S13 compares the second cyclic voltammetry (CV) curves of the α-$K_{0.19}MnO_2$ and α-$K_{0.07}MnO_2$ cathodes in aqueous 3 M $Zn(CF_3SO_3)_2$ with 0.2 M $Mn(CF_3SO_3)_2$ electrolyte. The CV curve of α-$K_{0.19}MnO_2$ shows two cathodic peaks located at 1.38 and 1.10 V and an overlapped anodic peak at 1.57 and 1.62 V, while that of α-$K_{0.07}MnO_2$ displays cathodic peaks at 1.35 and 1.05 V and an overlapped anodic peak at 1.61 and 1.67 V. This slight change suggests that the H^+/Zn^{2+} intercalation/deintercalation processes in the α-$K_{0.19}MnO_2$ show improved.

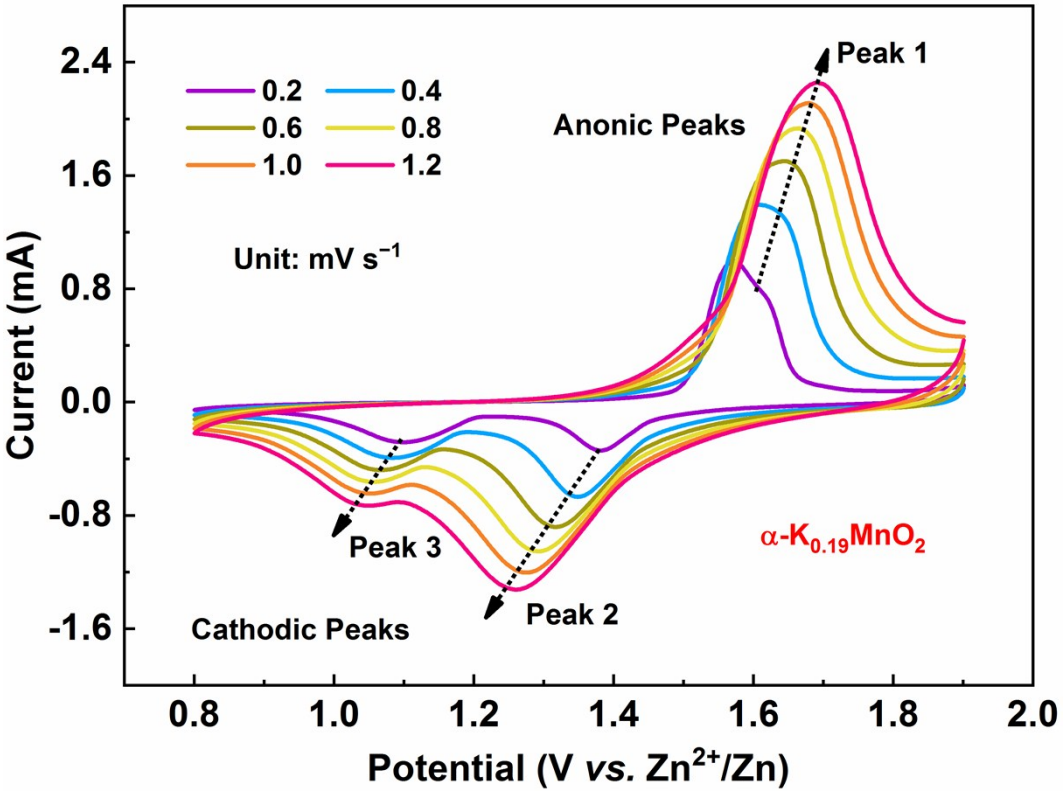

Fig. S14 CV curves of α-$K_{0.19}MnO_2$ cathodes at different scan rates in 3 M $Zn(CF_3SO_3)_2$ and 0.2 M $Mn(CF_3SO_3)_2$ electrolyte.

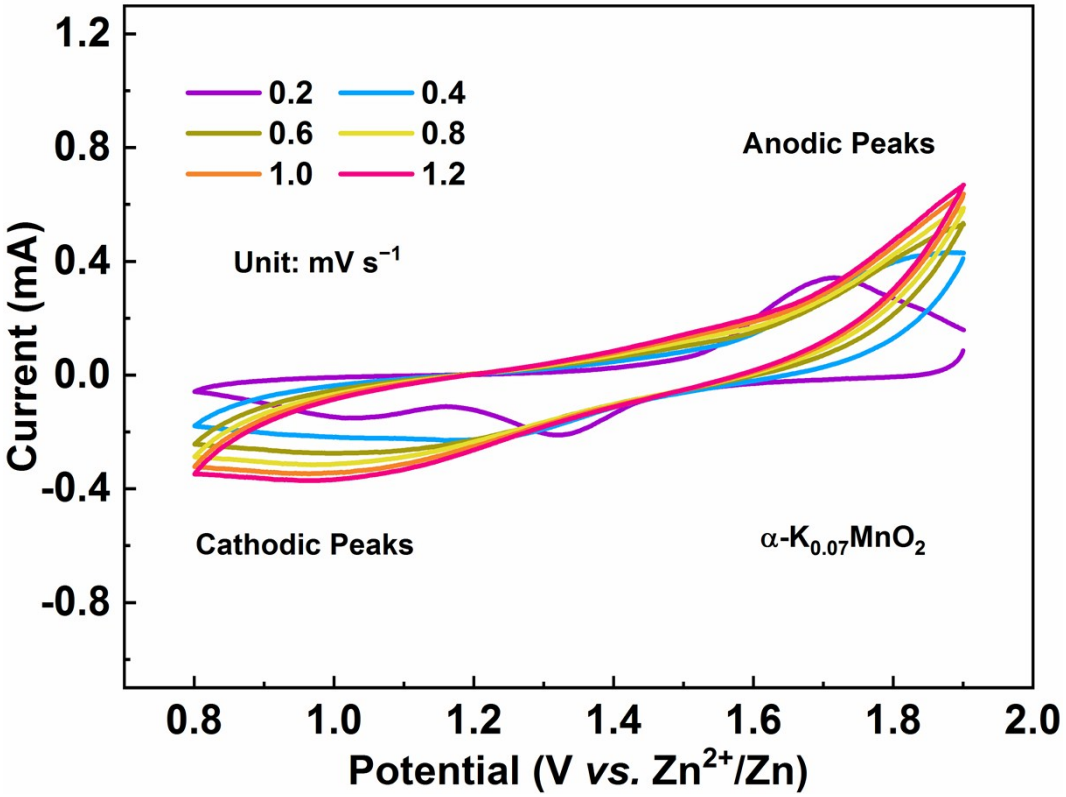

Fig. S15 CV curves of α-$K_{0.07}MnO_2$ cathodes at different scan rates in 3 M $Zn(CF_3SO_3)_2$ and 0.2 M $Mn(CF_3SO_3)_2$ electrolyte.

The CV curves of the α-$K_{0.07}MnO_2$ cathodes at various scan rates are shown in **Fig. S15**. With the increase of scan rates, the shape of the redox peaks is well maintained under slow scan rates, while the shape of the redox peaks has some changes under fast scan rates, indicating that ion diffusion into the inside of α-$K_{0.07}MnO_2$ nanotubes is hindered or results the structure collapse under fast scan rates.

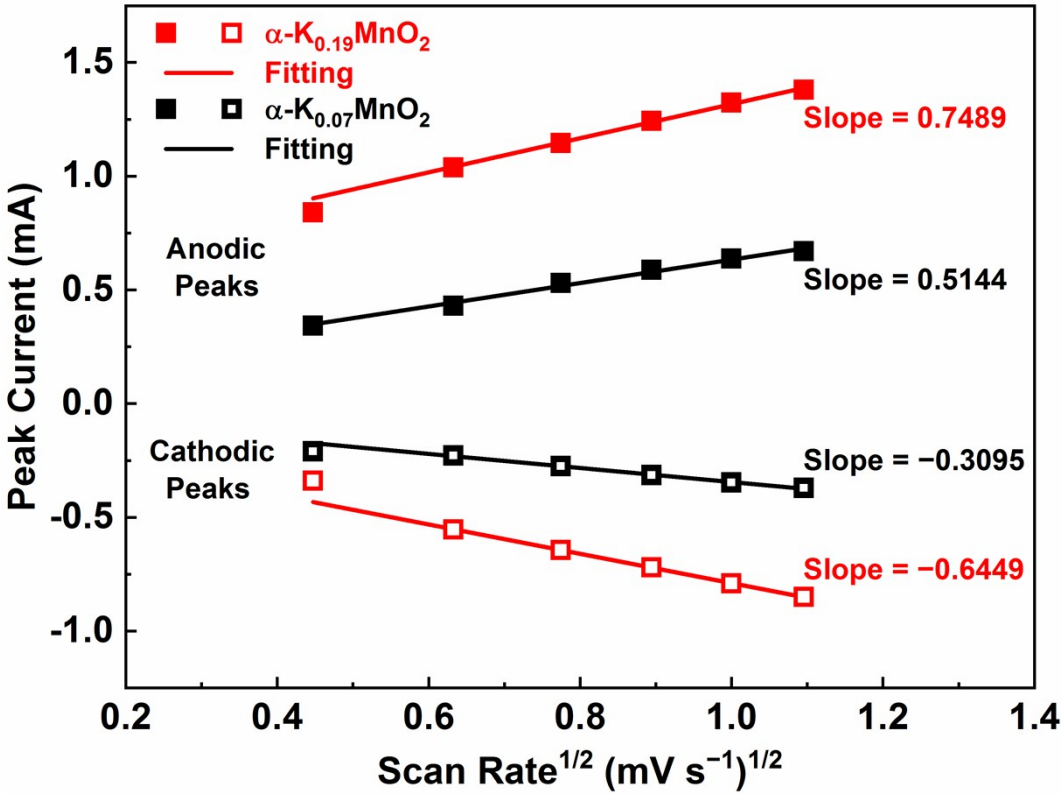

Fig. S16 The corresponding plots of peak currents with respect to the square root of scan rates of α-$K_{0.19}MnO_2$ and α-$K_{0.07}MnO_2$ cathodes.

Fig. S14−15 show the CV curves of the α-$K_{0.19}MnO_2$ and α-$K_{0.07}MnO_2$ cathodes at various scan rates ranging from 0.2 to 1.2 mV s^{-1}. With elevated scan rates, the currents of the redox peaks in the CV curves increase on the α-$K_{0.19}MnO_2$ cathode, while the shapes of the redox peaks are well maintained with slight shifts. The peak currents (i) have a power law relationship with the scan rates (v), which can be applied to analyze the detailed kinetics as follows: [S2,S3]

$$i = av^b \quad (1)$$

where a and b denote adjustable parameters. The b value for an ion insertion/extraction process is distinct from that of a process with capacitive behavior. Generally, a b value of 0.5

represents an ionic diffusion-controlled process, while a value of 1 indicates a capacitive process controlled by a surface electrochemical reaction. The redox peak currents (i_p) of α-$K_{0.19}MnO_2$ and α-$K_{0.07}MnO_2$ cathodes are proportional to the square root of the scan rate ($v^{1/2}$) suggesting that the electrochemical reaction of the α-$K_{0.19}MnO_2$ cathode is controlled by ionic diffusion, as shown in **Fig. S16**, and the slopes of the α-$K_{0.19}MnO_2$ cathode are steeper than those of the α-$K_{0.07}MnO_2$ cathode, indicating the faster ions diffusion into α-$K_{0.19}MnO_2$ nanotubes than that into α-$K_{0.07}MnO_2$ nanotubes.[S3]

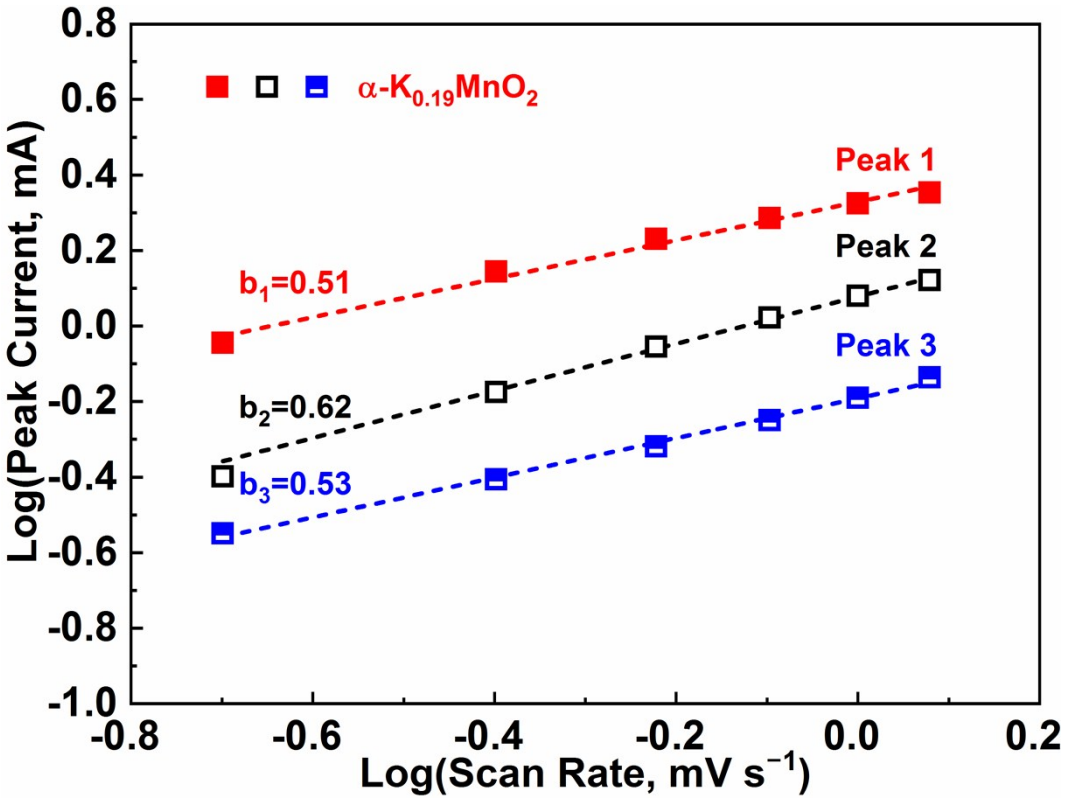

Fig. S17 The corresponding plots of log (peak current) *vs.* log (scan rate) of α-$K_{0.19}MnO_2$ cathodes.

The values of b for peaks 1, 2, and 3 were calculated to be 0.51, 0.62, and 0.53, respectively (**Fig. S17**). The values are approximately to 0.5, which further confirms that ion diffusion into the MnO_2 hosts is the rate-determining step in the case.

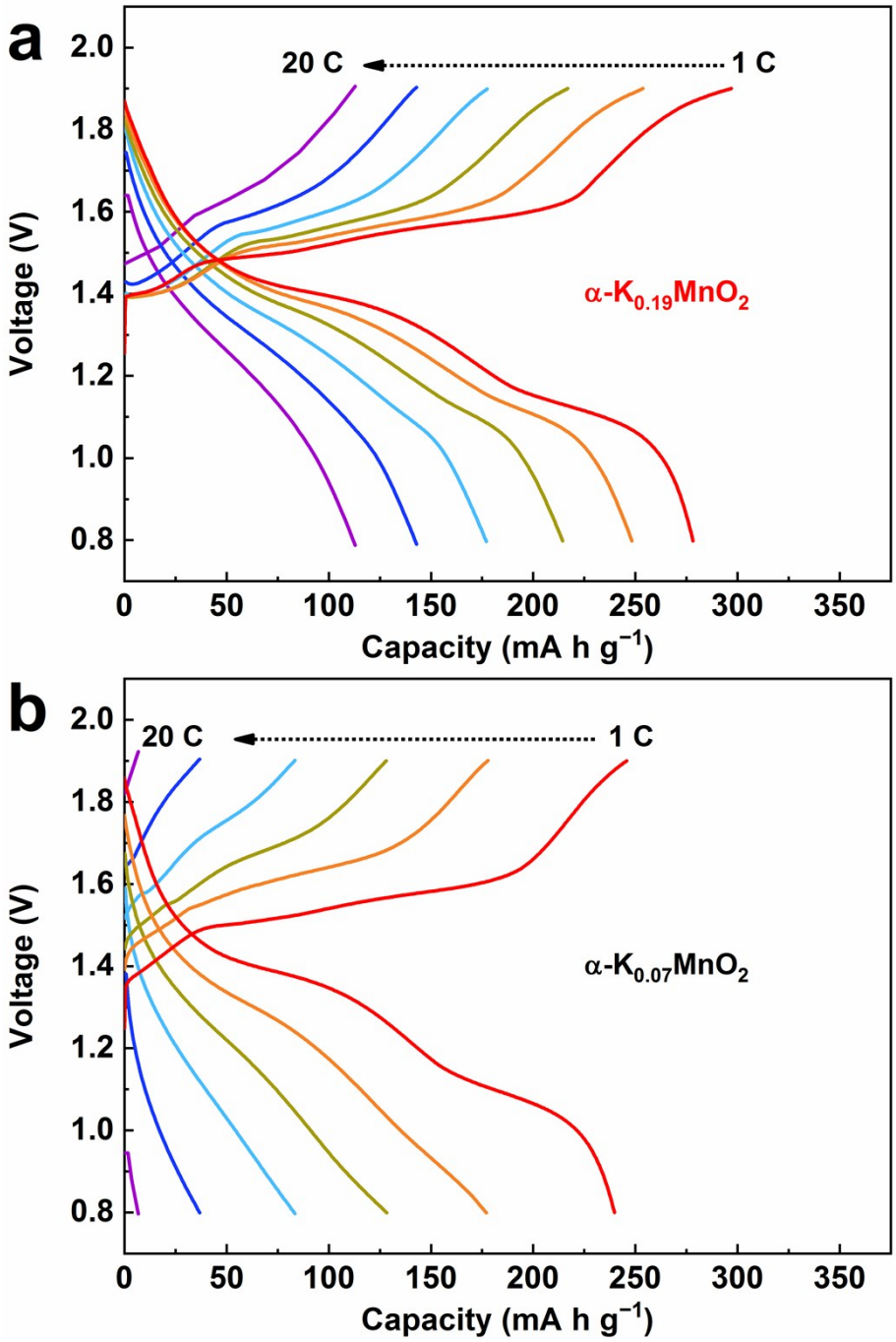

Fig. S18 (a) Rate perfornance of α-$K_{0.19}MnO_2$ cathodes and (b) Rate perfornance of α-$K_{0.07}MnO_2$ cathodes in 3 M $Zn(CF_3SO_3)_2$ and 0.2 M $Mn(CF_3SO_3)_2$ electrolyte.

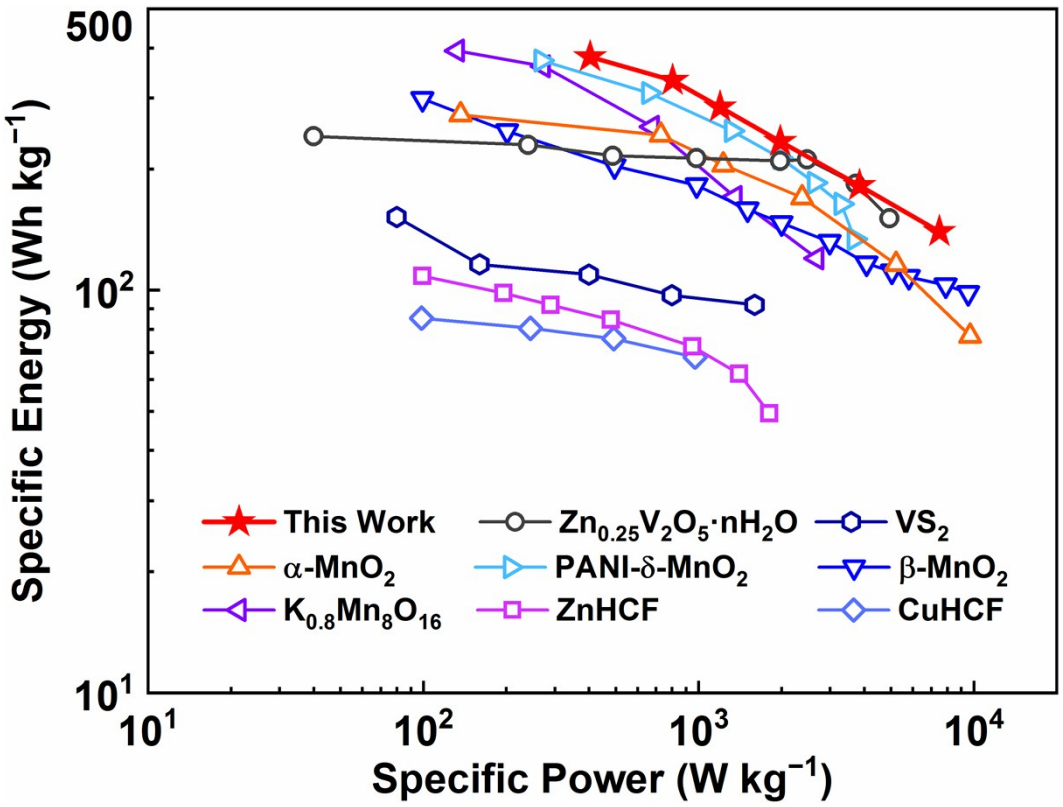

Fig. S19 The Ragone plots of Zn–α-$K_{0.19}MnO_2$ battery and ZIBs with other reported cathode materials. (Manganese-based materials: α-MnO_2,[S4] β-MnO_2,[S5] $K_{0.8}Mn_8O_{16}$,[S6] and PANI-δ-MnO_2;[S7] Vanadium-based materials: $Zn_{0.25}V_2O_5{\cdot}nH_2O$,[S8] and VS_2;[S9] Prussian blue analogues: ZnHCF,[S10] and CuHCF[S11])

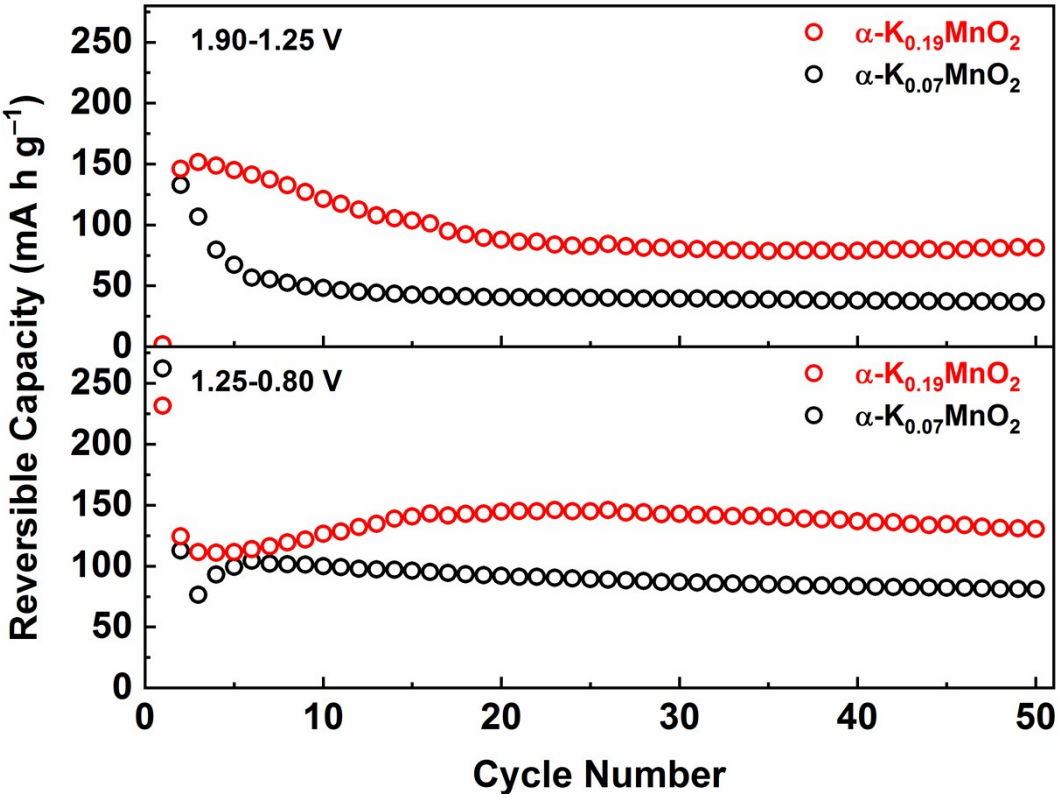

Fig. S20 Reversible (discharge) capacities *vs.* cycle number seperated from the potential range of 1.90–1.25 V and 1.25–0.80 V at 1 C of α-$K_{0.19}MnO_2$ and α-$K_{0.07}MnO_2$ cathodes in 3 M $Zn(CF_3SO_3)_2$ and 0.2 M $Mn(CF_3SO_3)_2$ electrolyte.

As shown in **Fig. S20**, the reversible capacities of the α-$K_{0.19}MnO_2$ cathode remain more stable than those of the α-$K_{0.07}MnO_2$ cathode during the two potential ranges, corresponding to H^+ and Zn^{2+} insertion processes, respectively. The stable cycling perforemances of α-$K_{0.19}MnO_2$ cathode could be attributed to the high K content in α-$K_{0.19}MnO_2$, which stabilizes the structure of MnO_2 through coordination of guest-ions with adjacent host atoms, thus providing a stable host for the ions insertion (H^+ and Zn^{2+}) and further promoting the cycling stability.

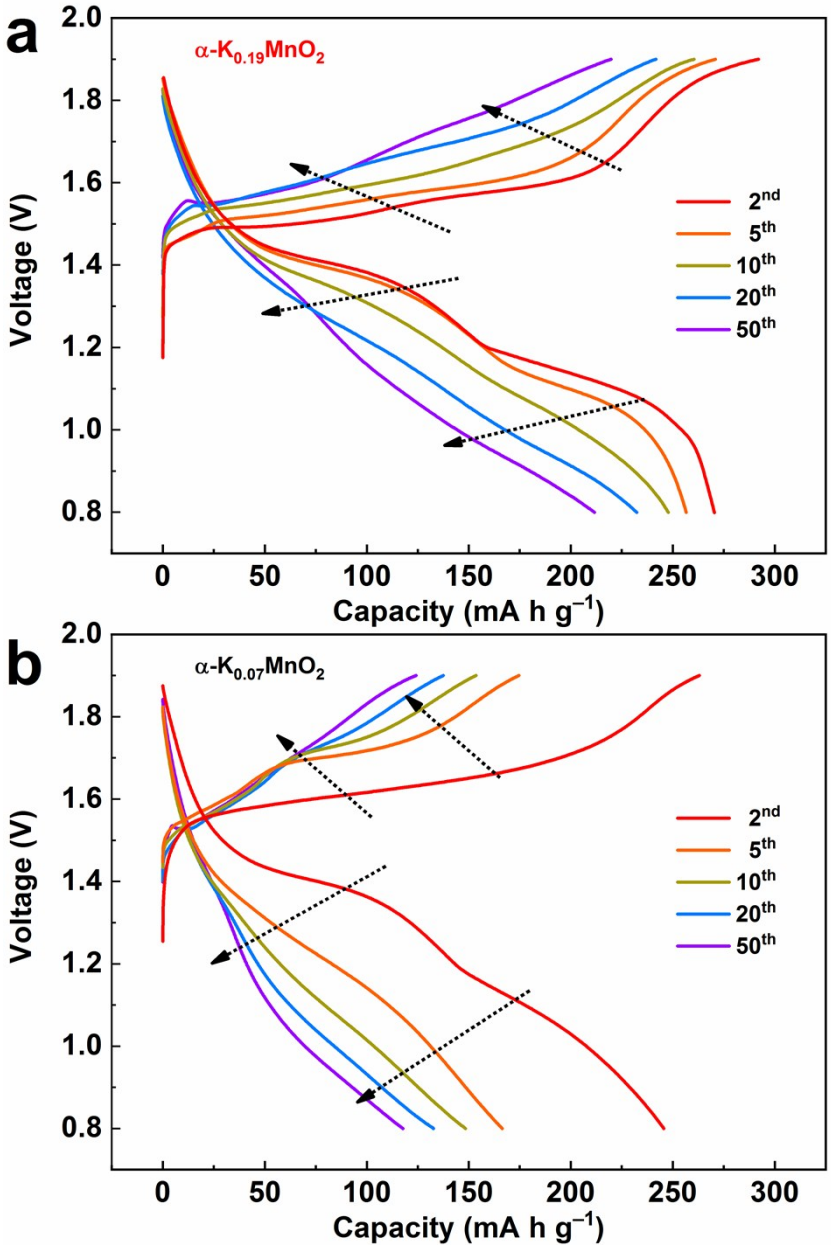

Fig. S21 (a) Discharge–charge curves of α-$K_{0.19}MnO_2$ cathodes and (b) discharge–charge curves of α-$K_{0.07}MnO_2$ cathodes at different cycles at 1 C.

The discharge–charge curves of α-$K_{0.19}MnO_2$ are relatively stable, while a rapid decrease in the discharge capacities is observed for α-$K_{0.07}MnO_2$. In addition, the discharge–charge platforms of α-$K_{0.19}MnO_2$ change relatively slowly than those of α-$K_{0.07}MnO_2$ with the increase of the cycling number. These results indicate that the high K content in α-$K_{0.19}MnO_2$ can reduce the barrier of H^+/Zn^{2+} insertion/extraction, which may be due to less structure damage and fewer irreversible reactions in α-$K_{0.19}MnO_2$ during the cycling.

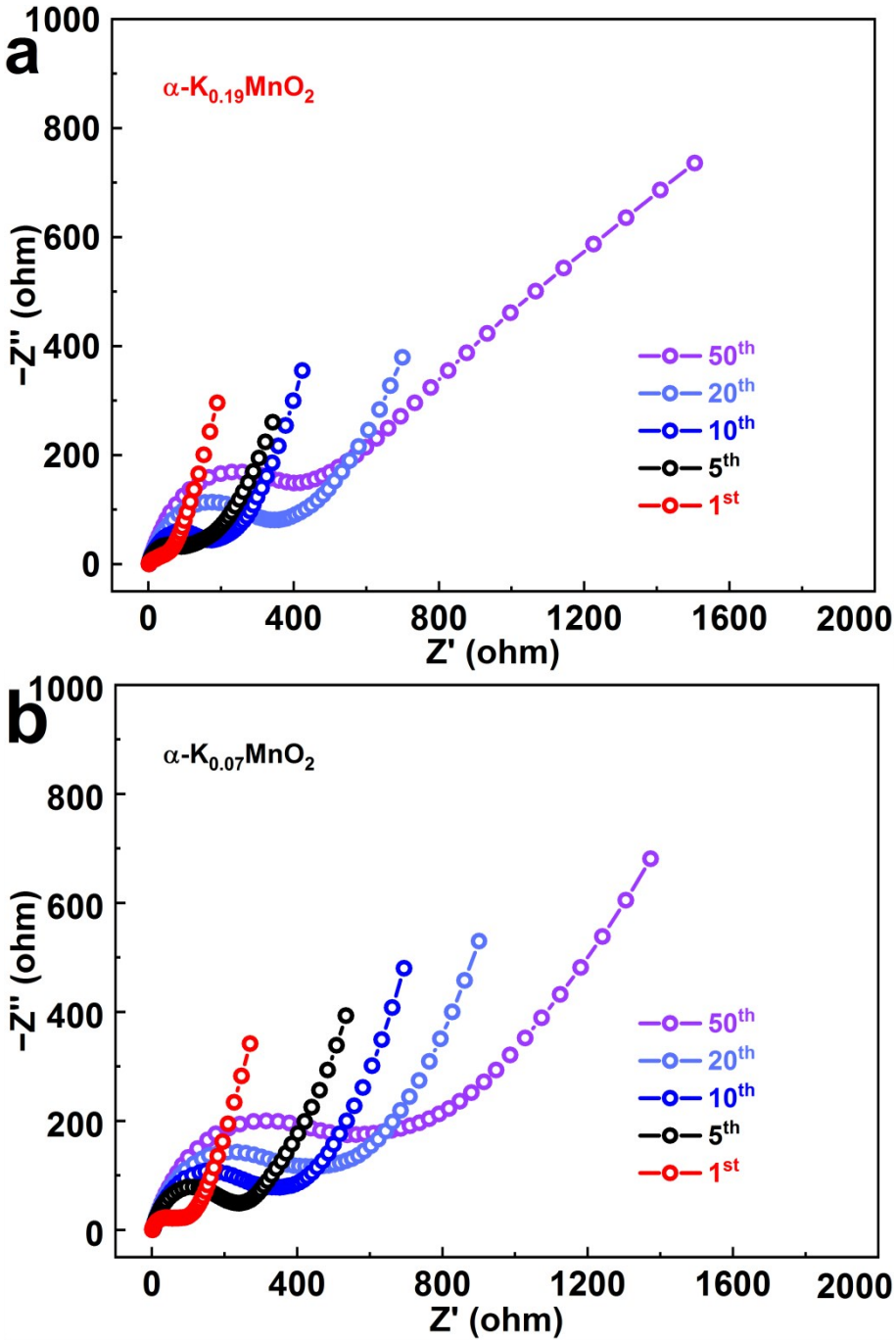

Fig. S22 (a) EIS analysis of α-$K_{0.19}MnO_2$ cathodes and (b) EIS analysis of α-$K_{0.07}MnO_2$ cathodes during cycling in 3 M $Zn(CF_3SO_3)_2$ and 0.2 M $Mn(CF_3SO_3)_2$ electrolyte.

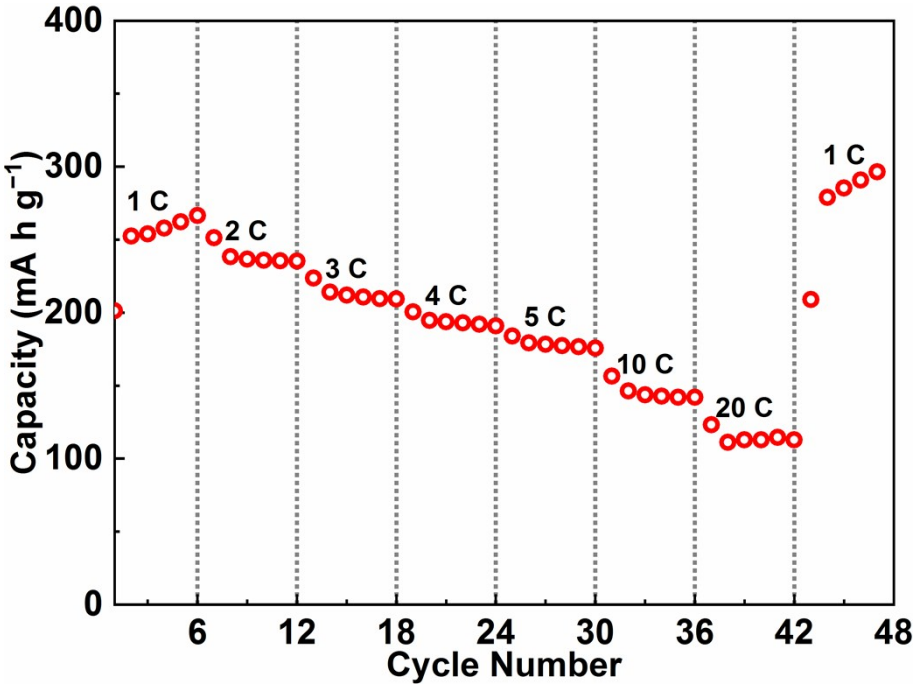

Fig. S23 Rate performance of α-$K_{0.19}MnO_2$ cathode in 3 M $Zn(CF_3SO_3)_2$ and 0.2 M $Mn(CF_3SO_3)_2$ electrolyte with 3 M $K(CF_3SO_3)$ as an additive.

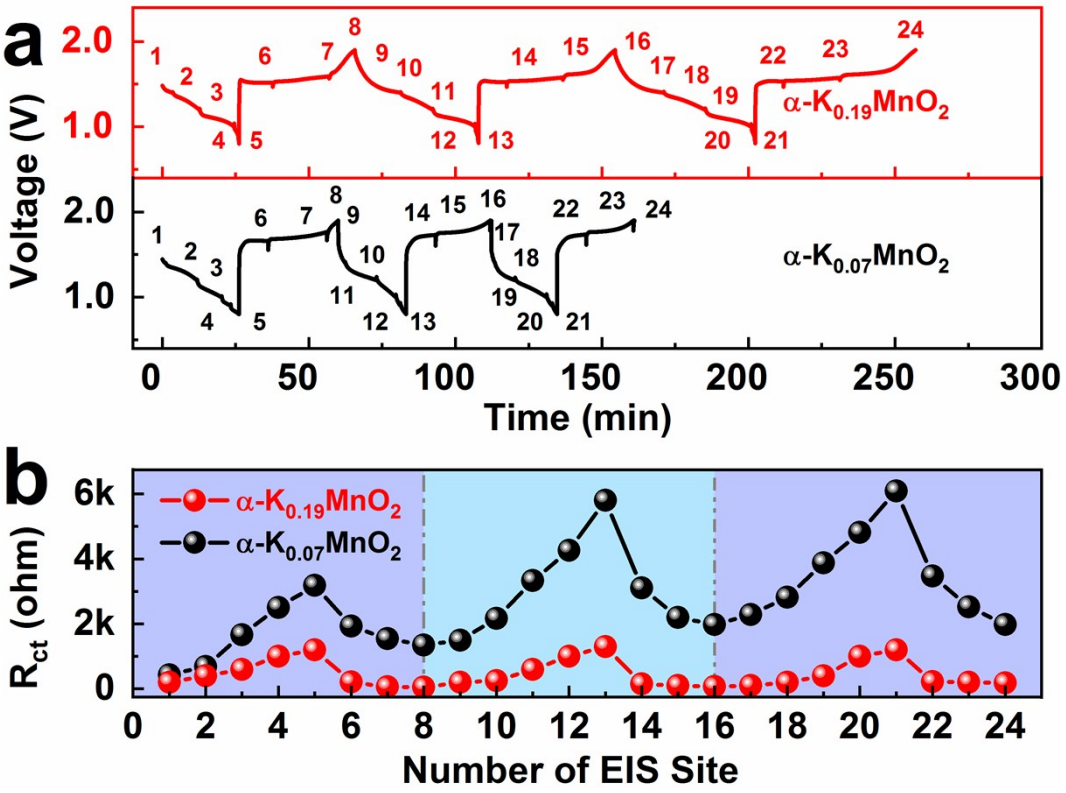

Fig. S24 (a) Discharge–charge curves (the marked consecutive numbers indicate the locations where EIS tests were recorded) and (b) the interface resistance evolution of the α-$K_{0.19}MnO_2$ and α-$K_{0.07}MnO_2$ cathodes during cycling.

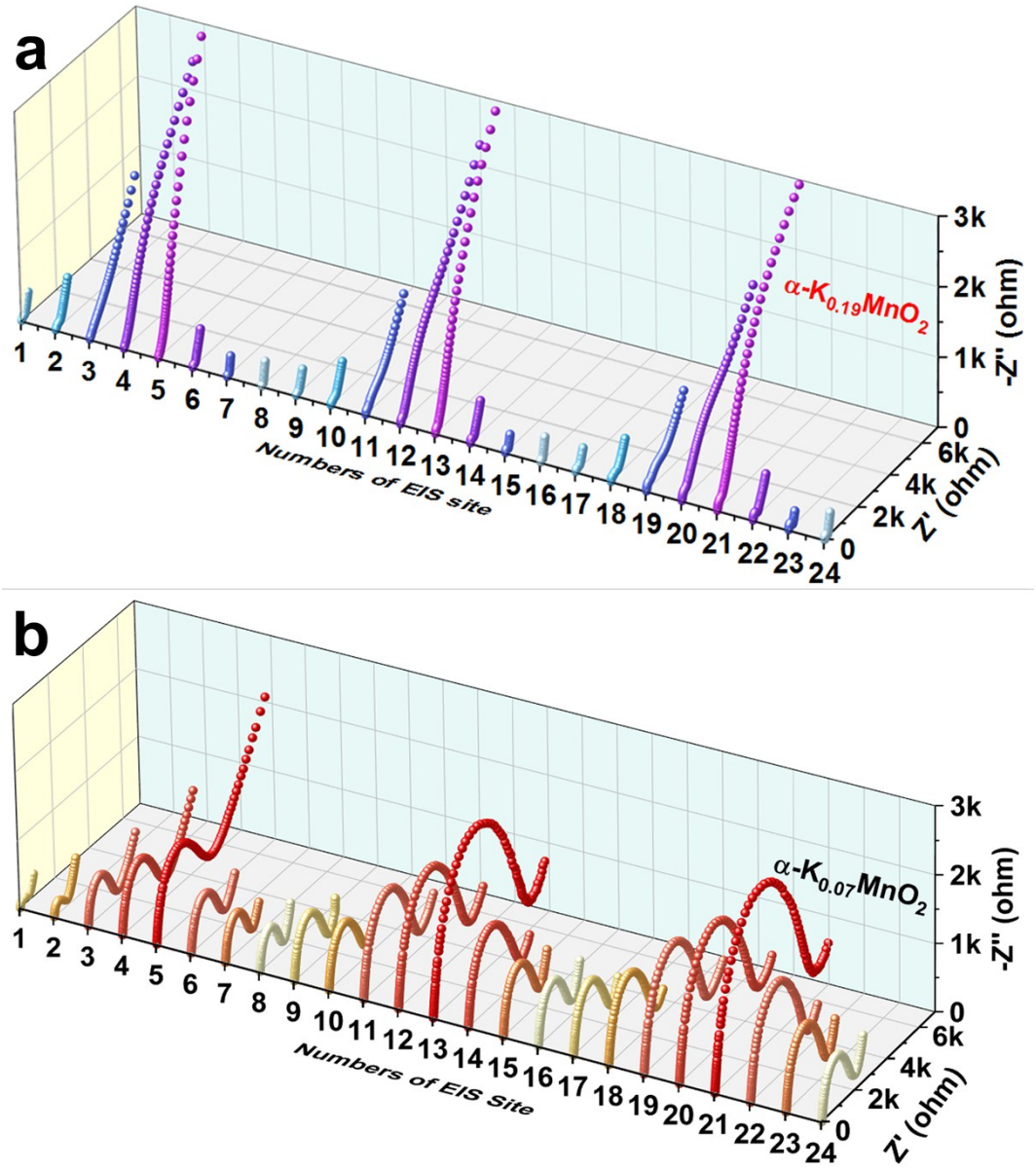

Fig. S25 (a) Nyquist plots of α-$K_{0.19}MnO_2$ cathodes. (b) Nyquist plots of α-$K_{0.07}MnO_2$ cathodes during the H^+/Zn^{2+} insertion and extraction in 3 M $Zn(CF_3SO_3)_2$ and 0.2 M $Mn(CF_3SO_3)_2$ electrolyte with 3 M $K(CF_3SO_3)$ electrolyte.

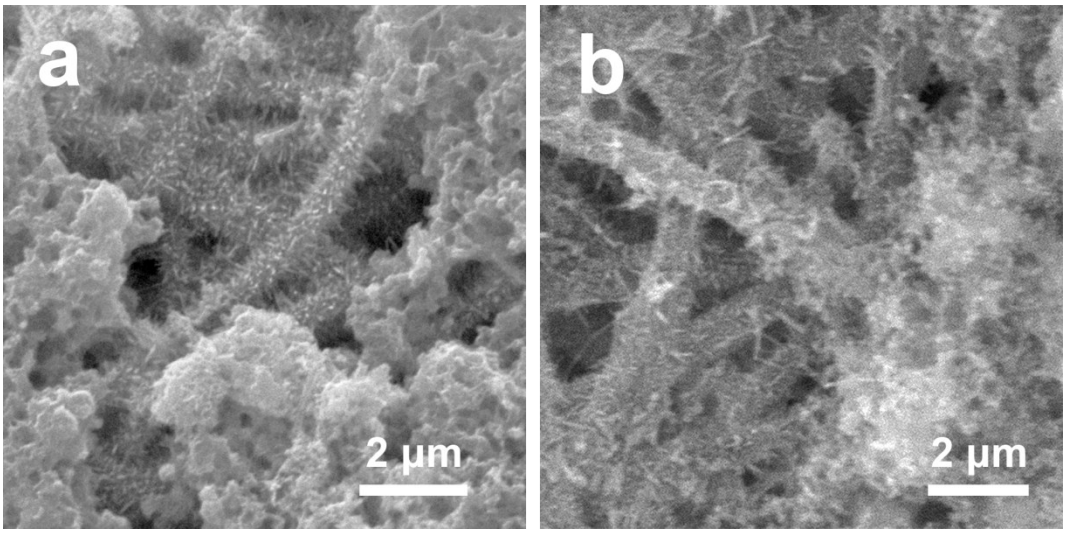

Fig. S26 (a) SEM image of α-$K_{0.19}MnO_2$ cathodes after cycling in 3 M $Zn(CF_3SO_3)_2$ and 0.2 M $Mn(CF_3SO_3)_2$ electrolyte with 3 M $K(CF_3SO_3)$ additive. (b) SEM image of α-$K_{0.19}MnO_2$ cathodes after cycling in 3 M $Zn(CF_3SO_3)_2$ and 0.2 M $Mn(CF_3SO_3)_2$ electrolyte.

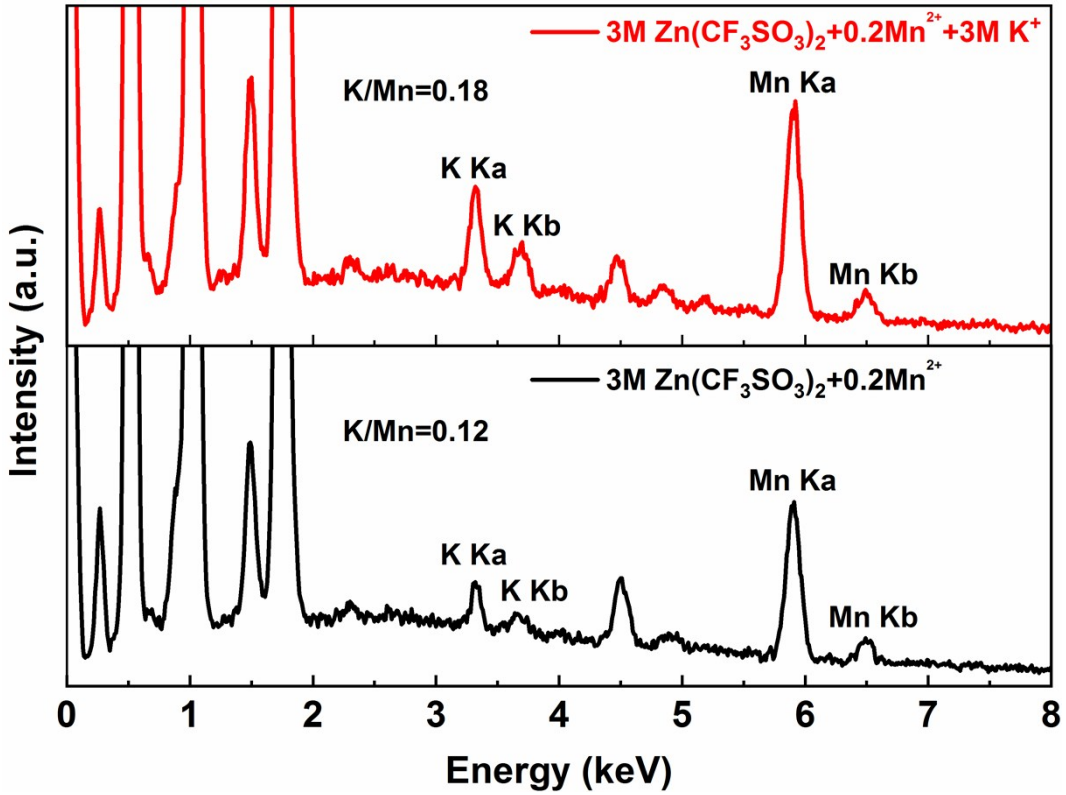

Fig. S27 EDX spectra of α-$K_{0.19}MnO_2$ cathodes after cycling in 3 M $Zn(CF_3SO_3)_2$ and 0.2 M $Mn(CF_3SO_3)_2$ electrolyte with/without 3 M $K(CF_3SO_3)$ (denoted as 3 M $Zn(CF_3SO_3)_2$ + 0.2 M Mn^{2+} + 3 M K^+ and 3 M $Zn(CF_3SO_3)_2$ + 0.2 M Mn^{2+}, respectively).

3. Supplementary Tables

Table S1 Chemical components of α-$K_{0.19}MnO_2$ and α-$K_{0.07}MnO_2$ nanotubes with EDX analysis.

Samples	O	Mn	K	K/M
α-$K_{0.19}MnO_2$	60.2	33.5	6.3	0.19
α-$K_{0.07}MnO_2$	62.8	34.9	2.3	0.07

Table S2 Chemical components of α-$K_{0.19}MnO_2$ and α-$K_{0.07}MnO_2$ nanotubes with ICP-OES analysis.

Samples	Mn	K	K/M
α-$K_{0.19}MnO_2$	84.1	15.9	0.19
α-$K_{0.07}MnO_2$	93.3	6.7	0.07

Table S3 Transport properties derived from the impedance spectra with EIS analysis.

Samples	R_e (Ω)	R_{ct} (Ω)	σ (Ω $s^{-1/2}$)	D(cm^2 s^{-1})
α-$K_{0.19}MnO_2$	0.89	16.7	23.8	2.60×10^{-13}
α-$K_{0.07}MnO_2$	1.16	51.8	44.4	7.48×10^{-14}

The R_e is ohmic resistance while the R_{ct} stands for charge-transfer resistance at interfaces. And the σ and D represent the Warburg coefficient and the chemical diffusion coefficient, respectively.

3. Supplementary References

S1 Y. Yuan, C. Zhan, K. He, H. Chen, W. Yao, S. Sharifi-Asl, B. Song, Z. Yang, A. Nie, X. Luo, H. Wang, S. M. Wood, K. Amine, M. S. Islam, J. Lu and R. Shahbazian-Yassar, *Nat. Commun.*, 2016, **7**, 13374.

S2 F. Wan, L. Zhang, X. Dai, X. Wang, Z. Niu and J. Chen, *Nat. Commun.*, 2018, **9**, 1656.

S3 X. Wang, Y. Xie, K. Tang, C. Wang and C. Yan, *Angew. Chem. Int. Ed.*, 2018, **57**, 11569−11573.

S4 C. Xu, B. Li, H. Du and F. Kang, *Angew. Chem. Int. Ed.*, 2012, **51**, 933−935.

S5 N. Zhang, F. Cheng, J. Liu, L. Wang, X. Long, X. Liu, F. Li and J. Chen, *Nat. Commun.*, 2017, **8**, 405.

S6 G. Fang, C. Zhu, M. Chen, J. Zhou, B. Tang, X. Cao, X. Zheng, A. Pan and S. Liang, *Adv. Funct. Mater.*, 2019, **29**, 1808375.

S7 J. Huang, Z. Wang, M. Hou, X. Dong, Y. Liu, Y. Wang and Y. Xia, *Nat. Commun.*, 2018, **9**, 2906.

S8 D. Kundu, B. D. Adams, V. Duffort, S. H. Vajargah and L. F. Nazar, *Nat. Energy*, 2016, **1**, 16119.

S9 P. He, M. Yan, G. Zhang, R. Sun, L. Chen, Q. An and L. Mai, *Adv. Energy Mater.*, 2017, **7**, 1601920.

S10 L. Zhang, L. Chen, X. Zhou and Z. Liu, *Adv. Energy Mater.*, 2015, **5**, 1400930.

S11 R. Trocoli and F. La Mantia, *ChemSusChem*, 2015, **8**, 481−485.